

Drivers of Precipitation Change: An Energetic Understanding

T. B. RICHARDSON,^a P. M. FORSTER,^a T. ANDREWS,^b O. BOUCHER,^c G. FALUVEGI,^{d,e} D. FLÄSCHNER,^f Ø. HODNEBROG,^g M. KASOAR,^h A. KIRKEVÅG,ⁱ J.-F. LAMARQUE,^j G. MYHRE,^g D. OLIVIÉ,ⁱ B. H. SAMSET,^g D. SHAWKI,^h D. SHINDELL,^k T. TAKEMURA,^l AND A. VOULGARAKIS^h

^a University of Leeds, Leeds, United Kingdom

^b Met Office Hadley Centre, Exeter, United Kingdom

^c Institut Pierre-Simon Laplace, Sorbonne Université, Paris, France

^d NASA Goddard Institute for Space Studies, New York, New York

^e Center for Climate Systems Research, Columbia University, New York, New York

^f Max-Planck-Institut für Meteorologie, Hamburg, Germany

^g Center for International Climate and Environmental Research, Oslo, Norway

^h Imperial College London, London, United Kingdom

ⁱ Norwegian Meteorological Institute, Oslo, Norway

^j NCAR/UCAR, Boulder, Colorado

^k Duke University, Durham, North Carolina

^l Kyushu University, Fukuoka, Japan

(Manuscript received 12 April 2017, in final form 1 September 2018)

ABSTRACT

The response of the hydrological cycle to climate forcings can be understood within the atmospheric energy budget framework. In this study precipitation and energy budget responses to five forcing agents are analyzed using 10 climate models from the Precipitation Driver Response Model Intercomparison Project (PDRMIP). Precipitation changes are split into a forcing-dependent fast response and a temperature-driven hydrological sensitivity. Globally, when normalized by top-of-atmosphere (TOA) forcing, fast precipitation changes are most sensitive to strongly absorbing drivers (CO₂, black carbon). However, over land fast precipitation changes are most sensitive to weakly absorbing drivers (sulfate, solar) and are linked to rapid circulation changes. Despite this, land-mean fast responses to CO₂ and black carbon exhibit more intermodel spread. Globally, the hydrological sensitivity is consistent across forcings, mainly associated with increased longwave cooling, which is highly correlated with intermodel spread. The land-mean hydrological sensitivity is weaker, consistent with limited moisture availability. The PDRMIP results are used to construct a simple model for land-mean and sea-mean precipitation change based on sea surface temperature change and TOA forcing. The model matches well with CMIP5 ensemble mean historical and future projections, and is used to understand the contributions of different drivers. During the twentieth century, temperature-driven intensification of land-mean precipitation has been masked by fast precipitation responses to anthropogenic sulfate and volcanic forcing, consistent with the small observed trend. However, as projected sulfate forcing decreases, and warming continues, land-mean precipitation is expected to increase more rapidly, and may become clearly observable by the mid-twenty-first century.

 Denotes content that is immediately available upon publication as open access.

 Supplemental information related to this paper is available at the Journals Online website: <https://doi.org/10.1175/JCLI-D-17-0240.s1>.

Corresponding author: T. B. Richardson, eetbr@leeds.ac.uk

1. Introduction

Understanding changes in the hydrological cycle is of great importance due to the potential impact on society (Alfieri et al. 2015). Precipitation is directly affected by



This article is licensed under a Creative Commons Attribution 4.0 license (<http://creativecommons.org/licenses/by/4.0/>).

individual forcing agents (Lambert and Faull 2007; Andrews et al. 2010; Kvalevåg et al. 2013) as well as global warming (Held and Soden 2006; Previdi 2010). This is because precipitation is tightly constrained by the atmospheric energy budget, such that globally the latent and sensible heat fluxes are balanced by net atmospheric radiative cooling (Mitchell et al. 1987; Allen and Ingram 2002; O’Gorman et al. 2012; Pendergrass and Hartmann 2014). As a result, the precipitation response to forcing can be split into a fast response, due to the near-instantaneous impact on the atmospheric energy budget, and a slow response, driven by surface temperature change (Bala et al. 2010; Andrews et al. 2010; Kvalevåg et al. 2013; Samset et al. 2016; MacIntosh et al. 2016; Sherwood et al. 2015). The fast precipitation response includes the direct radiative effects of the forcing agent, as well as any rapid adjustments of the troposphere and land surface.

The separation of fast and slow responses has significantly improved understanding of global precipitation changes, and the framework has been used to accurately emulate historical and twenty-first-century changes predicted by global climate models (Thorpe and Andrews 2014). However, uncertainties and intermodel differences in the precipitation response to forcing remain (Samset et al. 2016; Fläschner et al. 2016), particularly (but not only) for the effects of black carbon (Stjern et al. 2017). Uncertainty in the sensitivity of shortwave absorption to atmospheric water vapor is thought to drive significant model spread in the temperature-mediated precipitation response to forcing (DeAngelis et al. 2015). Improving understanding of the uncertainties and mechanisms involved is vital for improving prediction of future precipitation changes.

On local scales precipitation is strongly affected by circulation changes (Seager et al. 2010; Bony et al. 2013; Chadwick et al. 2013; Richardson et al. 2016a). Rapid circulation changes have been linked to changes in atmospheric absorption (Bony et al. 2013) as well as the rapid land surface response (Richardson et al. 2016a). Given the importance of the short-time-scale land surface response, forcings that have little effect on atmospheric absorption can still drive rapid spatial shifts in precipitation due to the surface forcing (Dong et al. 2014). Fast and slow precipitation responses have been shown to differ significantly over land and sea for many climate drivers (Samset et al. 2016; Shaw and Voigt 2015; M. J. Kim et al. 2016; Li and Ting 2017). It is important to understand the differing processes involved, particularly over land where changes will be most felt by society. The different regional responses can be analyzed energetically by taking into account horizontal energy transport as well as atmospheric cooling (Muller and O’Gorman 2011).

In this study we present the global, land, and sea mean precipitation and atmospheric energy budget responses

to five climate drivers (CO_2 , CH_4 , black carbon, sulfate, and insolation) across 10 global climate models participating in the Precipitation Driver Response Model Intercomparison Project (PDRMIP) (Myhre et al. 2017). The responses are split into fast and slow components. We analyze the atmospheric energy budget to understand the processes driving precipitation changes and isolate sources of uncertainty and intermodel spread. We use the PDRMIP results to construct a simple model for land-mean and sea-mean precipitation change based on sea-mean surface air temperature change and top-of-atmosphere (TOA) forcing. The simple model is used to emulate historical and future precipitation changes, and compared with CMIP5 output and observational records.

2. Methods

a. Data

We analyze data from 10 climate models (see Table S1 in the online supplemental material) participating in PDRMIP [see Myhre et al. (2017) for details]. Five abrupt forcing scenarios were implemented: doubling CO_2 concentration ($2\times\text{CO}_2$), tripling methane concentration ($3\times\text{CH}_4$), 5 times sulfate concentration or SO_2 emissions ($5\times\text{SO}_4$), 10 times black carbon concentration or emissions ($10\times\text{BC}$), and a 2% increase in insolation ($2\%\text{SOL}$). Perturbations are relative to either present-day or preindustrial values (see Table S1). Simulations were performed with fixed sea surface temperatures (fSST) for 15 years, and with a coupled ocean (coupled) for 100 years.

For models that were able to prescribe aerosol concentration fields, the baseline fields were constructed based on AeroCom Phase II (see Myhre et al. 2013a, 2017). In perturbed runs the baseline fields were scaled by the appropriate factors. In models for which this was not possible, the models native baseline emissions were scaled (see Table S1). The interactive chemistry in these models will introduce uncertainty across the responses.

Precipitation and near-surface air temperature data were obtained for 26 models (Table S2) participating in phase 5 of the Coupled Model Intercomparison Project (CMIP5) for the historical period (1850–2005) and two representative concentration pathway (RCP) scenarios out to 2100: RCP4.5 and RCP8.5 (Meinshausen et al. 2011). Two monthly precipitation observational datasets are used: the Global Precipitation Climatology Centre (GPCC) full data reanalysis version 7.0 at 0.5° resolution (1901–2013) (Becker et al. 2013) and the Climatic Research Unit time series (CRU TS) version 3.23 at 0.5° resolution (1901–2014) (Harris et al. 2014). Annual HadSST3 observational time series data are used to

provide global mean sea surface temperature from 1901 to 2015 (Morice et al. 2012).

b. Fast response and hydrological sensitivity

The precipitation response in the PDRMIP experiments is split into a fast component, due to near-instantaneous changes in the atmospheric energy budget, and a slow component, which scales with global mean surface temperature change. Following Richardson et al. (2016b), the fast response (P_{fast}) is calculated using fSST simulations (mean difference between perturbed and control simulations for years 2–15). The slow response is normalized by global mean surface temperature change (referred to as the hydrological sensitivity) and calculated using Eq. (1):

$$\text{HS} = \frac{P_{\text{tot}} - P_{\text{fast}}}{T_{\text{tot}} - T_{\text{fast}}}, \quad (1)$$

where HS is the hydrological sensitivity, P_{tot} is the total precipitation response, P_{fast} is the fast precipitation response, T_{tot} is the total coupled global-mean surface air temperature response, and T_{fast} is the fSST global-mean surface air temperature response (due to land surface adjustment). The total coupled response is taken as the mean difference between perturbed and control simulations for years 51–100 after the abrupt forcing is imposed. It should be noted that our definition of the hydrological sensitivity differs from the apparent hydrological sensitivity, as defined in Fläschner et al. (2016), which is commonly referred to in papers (e.g., Held and Soden 2006; Pendergrass and Hartmann 2014; Samset et al. 2016), and incorporates the fast component.

c. Atmospheric energy budget

To understand the precipitation responses we analyze the atmospheric energy budget, which provides constraints on precipitation. Globally, the latent heat released by precipitation is balanced by net atmospheric cooling. On local scales horizontal energy transport must be taken into account. Following Muller and O’Gorman (2011) we introduce a dry static energy (DSE) flux divergence term, as shown in Eq. (2):

$$L_c \delta P = \delta Q + \delta H = \delta \text{LWC} - \delta \text{SWA} - \delta \text{SH} + \delta H, \quad (2)$$

where δ denotes a perturbation, L_c is the latent heat of condensation, P is precipitation, Q is net atmospheric cooling, H is DSE flux divergence, LWC is atmospheric longwave cooling, SWA is atmospheric shortwave absorption, and SH is sensible heat flux from the surface.

Changes in H can be split into mean (H_m) and eddy (H_{trans}) components. Changes in H_m can be decomposed

into four components associated with dynamic and thermodynamic effects on the horizontal and vertical advection of DSE, as shown in Eq. (3):

$$\begin{aligned} H_m &= \delta H_{\text{Dyn}_v} + \delta H_{\text{Thermo}_v} + \delta H_{\text{Dyn}_h} + \delta H_{\text{Thermo}_h} \\ &= \int \delta(\bar{\omega}) \frac{\partial \bar{s}}{\partial p} + \int \bar{\omega} \delta \left(\frac{\partial \bar{s}}{\partial p} \right) + \int \delta(\bar{\mathbf{u}}) \cdot \nabla \bar{s} + \int \bar{\mathbf{u}} \cdot \delta(\nabla \bar{s}), \end{aligned} \quad (3)$$

where H_m is the mean component of DSE flux divergence, ω is vertical velocity, s is dry static energy, p is pressure, \mathbf{u} is the horizontal wind vector, ∇ is the horizontal gradient, overbars denote climatological monthly means, δ denotes a perturbation, and \int denotes mass-weighted vertical integration over the column as shown in Eq. (4):

$$\int = \int \frac{dp}{g}, \quad (4)$$

where p is pressure and g is acceleration due to gravity. Note that H_{Dyn_v} is associated with changes in vertical velocity, H_{Thermo_v} is associated with changes in vertical DSE gradients, H_{Dyn_h} is associated with changes in horizontal winds, and H_{Thermo_h} is associated with changes in horizontal DSE gradients.

Equation (2) is used to analyze the precipitation responses over land and sea across PDRMIP models, with H calculated as a residual. For one model (HadGEM2), for which the required data are available, we calculate H_m explicitly and analyze the separate components outlined in Eq. (3). Changes in H_{trans} are calculated as a residual.

Energy budget components are also split into a fast response (including the direct radiative effects of forcing agents as well as any rapid adjustments) and a temperature-driven response, using the same methods as for precipitation [see section 2b, Eq. (1)].

d. Simple precipitation model

Using the PDRMIP output we construct a simple model for land-mean and sea-mean precipitation change based upon the fast and slow response framework. Precipitation change is estimated using a linear combination of forcing-dependent fast components, and a sea surface temperature-dependent response, as shown in Eqs. (5) and (6):

$$\delta P_L(t) = \sum_i R_{L_i} F_i(t) + \text{HS_SST}_L \times \delta \text{SST}(t), \quad (5)$$

$$\delta P_S(t) = \sum_i R_{S_i} F_i(t) + \text{HS_SST}_S \times \delta \text{SST}(t), \quad (6)$$

where $\delta P_L(t)$ [or $\delta P_S(t)$] is the change in land (or sea) mean precipitation at time t , $F_i(t)$ is the global mean

TABLE 1. Contributions to land- and sea-mean precipitation change relative to preindustrial due to fast responses to climate forcings and surface temperature change calculated using the simple model. Results are given for the period 1991–2000 and 2091–2100 for RCP4.5 and RCP8.5. All values are given in mm yr^{-1} . The uncertainties take into account intermodel spread and uncertainty in the historical forcings, as described in section 2d. (Sol is solar insolation; Vol is volcano activity.)

	Land			Sea		
	1991–2000	2091–2100 (RCP4.5)	2091–2100 (RCP8.5)	1991–2000	2091–2100 (RCP4.5)	2091–2100 (RCP8.5)
δP	$-5.5^{+7.4}_{-10.7}$	23.3 ± 8.1	47.5 ± 14.4	$-1.0^{+8.9}_{-8.2}$	47.9 ± 7.8	86.3 ± 12.4
Temperature	7.1 ± 1.1	26.9 ± 3.7	48.7 ± 6.4	25.2 ± 2.7	95.1 ± 7.5	172 ± 11.8
CO ₂	0.2 ± 1.8	0.57 ± 4.7	1.0 ± 8.5	-13.6 ± 1.5	-36.2 ± 1.3	-65.4 ± 2.3
CH ₄	1.9 ± 0.5	1.7 ± 0.4	4.6 ± 1.1	-4.1 ± 0.7	-3.6 ± 0.5	-9.9 ± 1.2
SO ₄ +CA	$-10.9^{+6.4}_{-10.0}$	-4.3 ± 0.8	-5.3 ± 0.8	$1.4^{+0.9}_{-1.3}$	0.3 ± 0.4	0.3 ± 0.4
BC	$-1.0^{+1.2}_{-1.1}$	-0.5 ± 0.3	-0.5 ± 0.3	$-7.3^{+7.3}_{-6.4}$	-3.4 ± 0.2	-3.7 ± 0.2
Sol	0.4 ± 0.37	0.4 ± 0.02	0.4 ± 0.02	-0.3 ± 0.28	-0.3 ± 0.01	-0.3 ± 0.01
Vol	-3.3 ± 1.2	-1.6 ± 0.08	-1.6 ± 0.08	82.4 ± 0.9	1.2 ± 0.04	1.2 ± 0.04

TOA forcing for a given climate driver i at time t , and $\delta\text{SST}(t)$ is the change in sea-mean surface air temperature at time t ; R_{L_i} (or R_{S_i}) is the land-mean (or sea-mean) fast precipitation response normalized by TOA forcing for a given climate driver i . The R factors (shown in Table S3) are calculated from the PDRMIP simulations as shown in Eqs. (7) and (8):

$$R_L = P_{\text{fast}_L} / F \quad (7)$$

$$R_S = P_{\text{fast}_S} / F \quad (8)$$

where P_{fast_L} and P_{fast_S} are, respectively, the land-mean and sea-mean fast precipitation response, and F is the global-mean TOA forcing. The terms HS_SST_L and HS_SST_S are respectively the land-mean and sea-mean hydrological sensitivity calculated with respect to sea-mean surface air temperature. The simple model uses a hydrological sensitivity that scales with sea surface temperature so that the land surface temperature change that occurs in the fSST simulations is not double counted. For each model, the hydrological sensitivity is taken as the mean of the $2 \times \text{CO}_2$, $5 \times \text{SO}_4$, and $2\% \text{SOL}$ experiments ($10 \times \text{BC}$ and $3 \times \text{CH}_4$ are not included as they produce little surface temperature change). The PDRMIP multimodel-mean HS_SST_L and HS_SST_S are then used for the simple model (Table S3). It should be noted that H is included in both terms on the right-hand side of Eqs. (5) and (6).

The simple model is used to estimate historical and future precipitation change following RCP4.5 and RCP8.5. The F_i time series data (Fig. S1) are taken from Meinshausen et al. (2011). The δSST time series data are taken as the CMIP5 ensemble mean. The black carbon forcing time series includes only direct radiative effects. Sulfate direct radiative forcing is grouped with cloud albedo (indirect) forcing. Other aerosol species will contribute to the cloud albedo changes, but sulfate is

consistently found to dominate aerosol indirect effects on clouds (Takemura 2012; Shindell et al. 2013).

As well as the five PDRMIP drivers, forcings due to volcanoes and greenhouse gases (GHGs) other than CO_2 and CH_4 are included in the simple model. Volcanic forcing is assumed to have the same R factor as $2\% \text{SOL}$, as the predominant effect is a reduction in incoming solar irradiance (Myhre et al. 2013b). GHGs apart from CH_4 are assumed to have the same R factor as CO_2 , as they affect the atmospheric energy budget through the same mechanism of LW absorption. Given that CO_2 dominates GHG forcing we do not expect this assumption to significantly affect the results. It should be noted that various forcings such as ozone, land-use change, and biomass burning are not included. The simple model is also compared against precipitation observations over land, using the HadsST3 dataset for the δSST input.

We compute a measure of the uncertainty associated with the simple model results (presented in Table 1). The uncertainty bounds are computed by propagating the following uncertainties associated with each term in Eqs. (6) and (7): 1) the standard error of the PDRMIP intermodel spread in the R factors, 2) the IPCC uncertainty ranges on historical forcing taken from Tables 8.2, 8.4, and 8.6 in Myhre et al. (2013b), 3) the standard error of the PDRMIP intermodel spread in HS_SST , and 4) the standard error of the CMIP5 intermodel spread in the historical and future temperature time series.

3. Results and discussion

a. Global fast response

We first decompose the multimodel global mean precipitation response to the five PDRMIP drivers into a fast component and hydrological sensitivity (Fig. 1). The fast

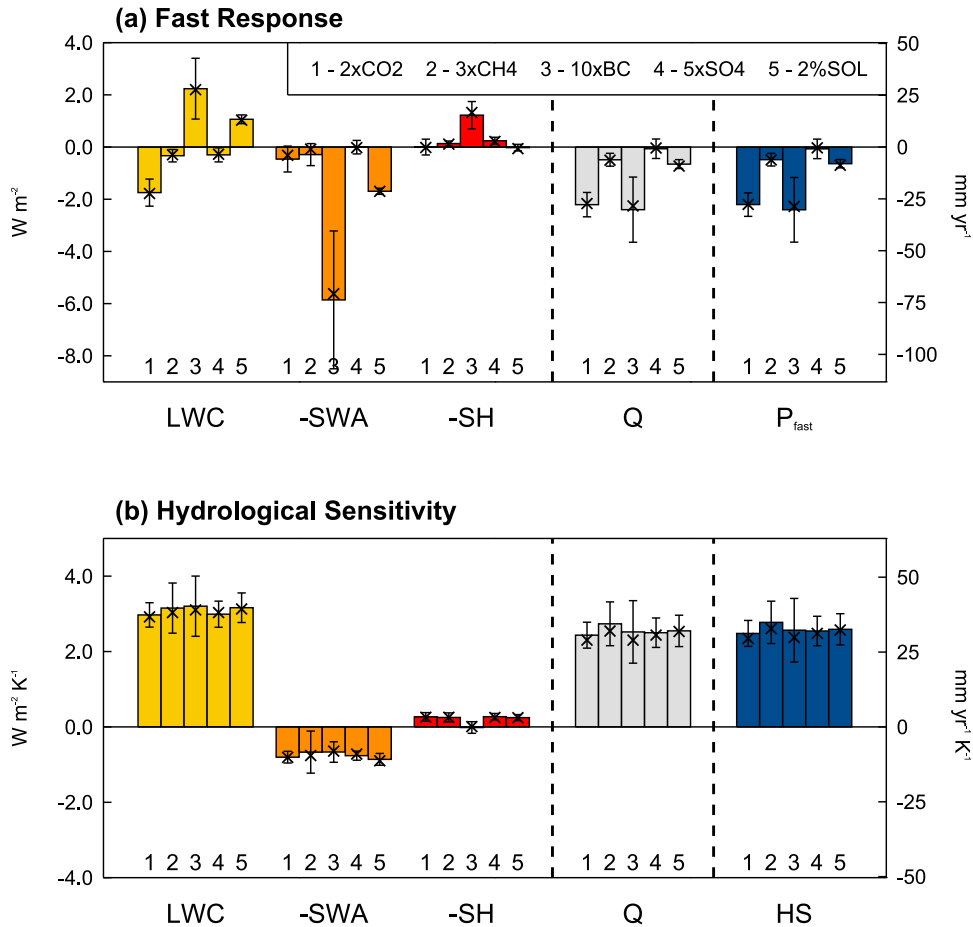


FIG. 1. Multimodel global mean (a) fast precipitation response (P_{fast} ; blue) and (b) hydrological sensitivity (HS; blue) in response to the five PDRMIP forcing scenarios; P_{fast} and HS are decomposed into the contributions from the atmospheric energy budget: net longwave cooling (LWC; yellow), net shortwave absorption (SWA, orange), sensible heat flux from the surface (SH; red), and the net atmospheric cooling (Q ; light gray). The sign of change in each component is given such that a positive value contributes positively to precipitation change. Results are shown in both energetic units (left axis) [W m^{-2} in (a) and $\text{W m}^{-2} \text{K}^{-1}$ in (b)] and precipitation units (right axis) [mm yr^{-1} in (a) and $\text{mm yr}^{-1} \text{K}^{-1}$ in (b)]. Error bars denote the standard deviation of model spread, and crisscrosses show the median value.

response (Fig. 1a) varies significantly between drivers, with $2\times\text{CO}_2$ and $10\times\text{BC}$ producing large reductions in precipitation consistent with previous single-model studies (Andrews et al. 2010; Kvilevåg et al. 2013).

The variation in fast responses can be explained through the impact of each forcing agent on the atmospheric energy budget (also shown in Fig. 1). Doubling CO_2 produces a large negative fast precipitation response associated with the reduction in atmospheric LW cooling. This is robust across the PDRMIP models (see Fig. S1a). The intermodel spread in SH flux change is well correlated with the intermodel spread in the fast precipitation response to CO_2 . The cross-model correlation between P_{fast} and SH flux [$r = -0.77$ (-0.27 to -0.94)] is considerably larger than for LW cooling or

SW absorption, both of which are statistically indistinguishable from zero. This is mainly attributable to the land surface response (see Fig. 2 and section 3c). Tripling methane produces a smaller reduction in net atmospheric cooling (Fig. 1a); however, the forcing is somewhat smaller for this scenario (Fig. S2). The fast CH_4 precipitation response per unit TOA forcing is more comparable to the CO_2 response (Fig. 3).

The $10\times\text{BC}$ experiment produces a large negative fast precipitation response associated with a substantial increase in atmospheric shortwave absorption (Fig. 1a). This is partially counteracted by increased LW cooling and a reduction in surface SH flux as the atmosphere warms. Per unit TOA forcing black carbon causes a fast precipitation response over 3.5 times larger than any

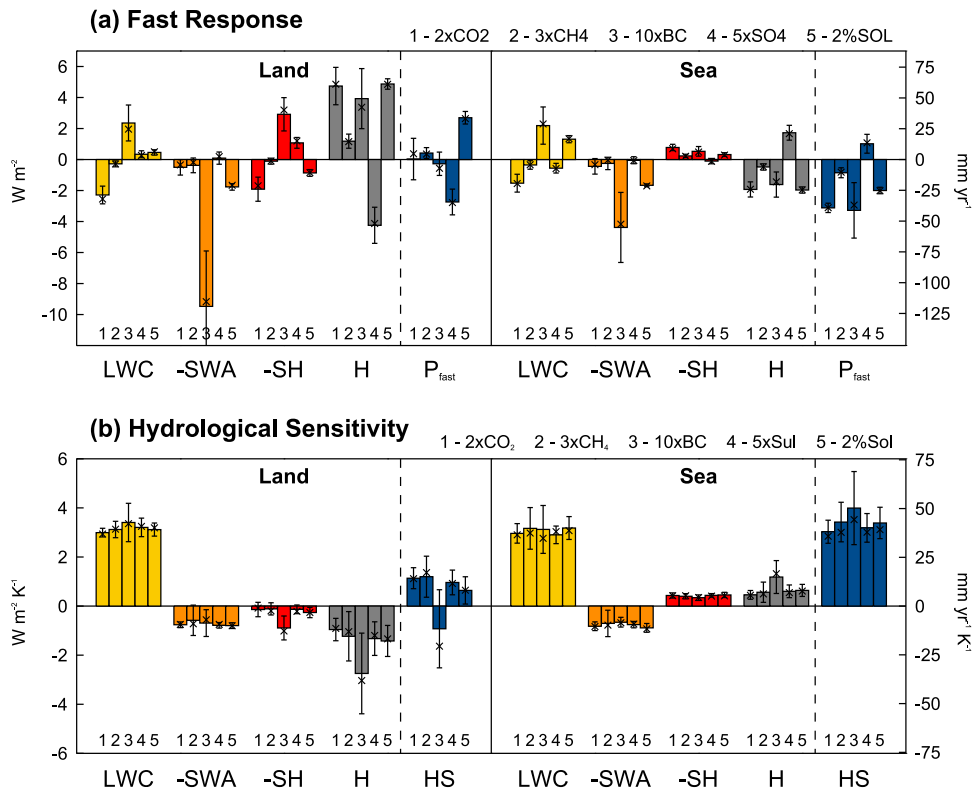


FIG. 2. Multimodel land and sea mean (a) fast precipitation response (P_{fast} ; blue) and (b) hydrological sensitivity (HS; blue) in response to the PDRMIP forcing scenarios; P_{fast} and HS are decomposed into the contributions from the local atmospheric energy budget: net longwave cooling (LWC; yellow), net shortwave absorption (SWA; orange), sensible heat flux from the surface (SH; red), and the DSE flux divergence (H ; dark gray). The hydrological sensitivity over land and sea is normalized by global mean temperature change. The sign of change in each component is given such that a positive value contributes positively to precipitation change. Results are shown in both energetic units (left axis) [W m^{-2} in (a) and $\text{W m}^{-2} \text{K}^{-1}$ in (b)] and precipitation units (right axis) [mm yr^{-1} in (a) and $\text{mm yr}^{-1} \text{K}^{-1}$ in (b)]. Error bars denote the standard deviation of model spread, and crisscrosses show the median value.

other driver (Fig. 3), associated with its strong impact on SW absorption. However, it should be noted that this result is likely to be sensitive to the vertical distribution of the black carbon perturbation. Previous work has shown different vertical profiles of black carbon can affect the relation between TOA forcing and atmospheric forcing, and hence precipitation (Ming et al. 2010). Given the large uncertainty associated with industrial era radiative forcing from black carbon (Bond et al. 2013; Samset et al. 2014; Boucher et al. 2016), and the complex relationship between BC forcing and surface temperature change (Chung et al. 2012; Bond et al. 2013; Myhre and Samset 2015), the influence on global precipitation is considerably more uncertain than for the other drivers.

The black carbon fast response exhibits considerable model spread (Fig. 1a), with the increase in SW absorption ranging from 2.9 to 10.3 W m^{-2} . The large spread mainly arises from the models with interactive

chemistry, which will affect how the emissions perturbation translates into concentration and atmospheric forcing. However, when normalized by TOA forcing the model spread in the fast precipitation response to black carbon is still considerably larger than for the other drivers (Fig. 3). This may be in part a result of differing vertical profiles of black carbon in the models with interactive chemistry.

Sulfate has very little impact on the net atmospheric cooling, and therefore produces a negligible global fast precipitation response (Fig. 1a). Increased solar irradiance causes a small negative fast response associated with increased atmospheric SW absorption (Fig. 1a), compensated partially by an increase in LW cooling.

b. Global hydrological sensitivity

The global hydrological sensitivity (Fig. 1b) is very consistent between drivers ranging from 31.2 to $34.9 \text{ mm yr}^{-1} \text{K}^{-1}$ (2.9%–3.2% K^{-1}). This lies at the higher

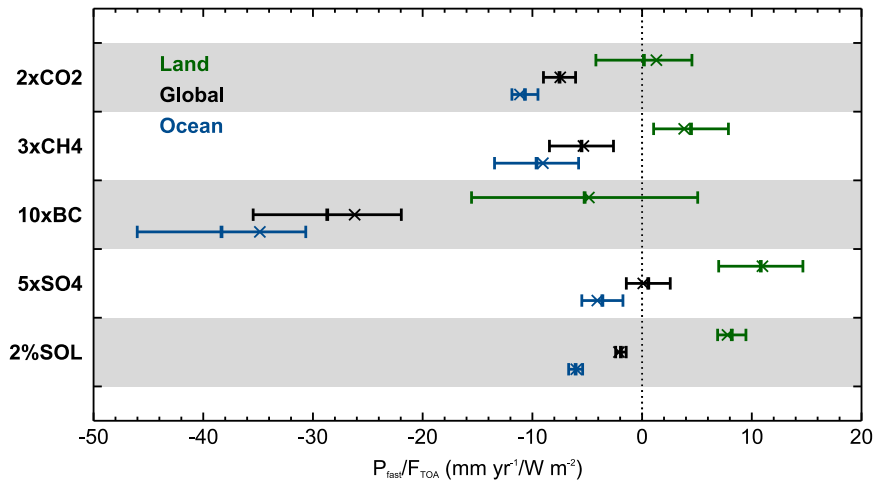


FIG. 3. Multimodel mean precipitation adjustment (P_{fast}) normalized by global mean TOA forcing (F_{TOA}) for the PDRMIP forcing scenarios. Results are shown for global (black), land (green), and ocean (blue) mean precipitation adjustments. The error bars denote the standard deviation of model spread, and the crisscrosses show the median value.

end of results from previous studies (Andrews et al. 2010; Kvalevåg et al. 2013; Fläschner et al. 2016). Differencing fSST and coupled simulations to calculate the hydrological sensitivity, as used in the present study, tends to produce higher values than regression techniques (Richardson et al. 2016b).

The hydrological sensitivity for all forcing scenarios is predominantly associated with an increase in LW cooling as the climate warms (Fig. 1b). The increased LW cooling is partially counteracted by a small increase in SW absorption, attributable to Clausius–Clapeyron-driven increases in water vapor. Surface sensible heat flux is affected very little by changing surface temperature. This is generally consistent across forcing scenarios and models. Intermodel spread in the hydrological sensitivity is highly correlated with the LW cooling feedback (Fig. 1b). For $2\times\text{CO}_2$ the cross-model correlation coefficient between the hydrological sensitivity and LW cooling [$r = 0.82$ (0.39 to 0.96)] is considerably larger than for SW absorption or SH flux, both of which are statistically indistinguishable from zero. This may be linked to uncertain cloud feedbacks that have little effect on atmospheric shortwave absorption (Lambert et al. 2014) but contribute strongly to intermodel spread in net atmospheric cooling (O’Gorman et al. 2012). Our results differ from previous studies that attribute a significant portion of the intermodel spread to shortwave absorption (Takahashi 2009; DeAngelis et al. 2015). Given that the radiation codes of the 10 models used in this study span 5 of the 7 examined in DeAngelis et al. (2015), it is likely that the difference arises due to different methodologies for separating the fast response and hydrological sensitivity.

Both Takahashi (2009) and DeAngelis et al. (2015) use regression techniques rather than separating the fast response using fSST simulations.

c. Fast response over land and sea

In Fig. 2, we split the precipitation and energy budget responses to forcing into land and sea means. It can be seen that the fast responses are very different over land and sea. In response to CO_2 the land mean fast precipitation response is negligible, whereas over the sea there is a reduction of -39.3 mm yr^{-1} (Fig. 2a). As seen for the global mean, over both land and sea doubling CO_2 causes a large reduction in atmospheric LW cooling. However, over land this is counteracted by changes in horizontal energy transport.

To help understand what drives the increase in DSE flux divergence over land, the separate components described in Eq. (3) are shown in Fig. 4 (and Fig. S3 for other forcing scenarios) for one model (HadGEM2). The increase in H over land is predominantly driven by an increase in $H_{\text{D}_{\text{yn},v}}$, associated with changes in vertical velocity. This indicates that increasing CO_2 enhances vertical motion over land, which is likely driven by the surface forcing. Higher CO_2 concentrations cause increased downwelling LW radiation at the surface (Fig. 5a). To restore balance, over land there is an increase in upwelling LW radiation and surface sensible heat flux (Fig. 5a). This will warm the lower troposphere, thus decreasing stability and driving enhanced convection and precipitation. This does not occur over the oceans where the sea surface temperature is fixed in these experiments (Fig. 6a). Therefore, the large negative fast precipitation response over the oceans is associated with increased atmospheric LW

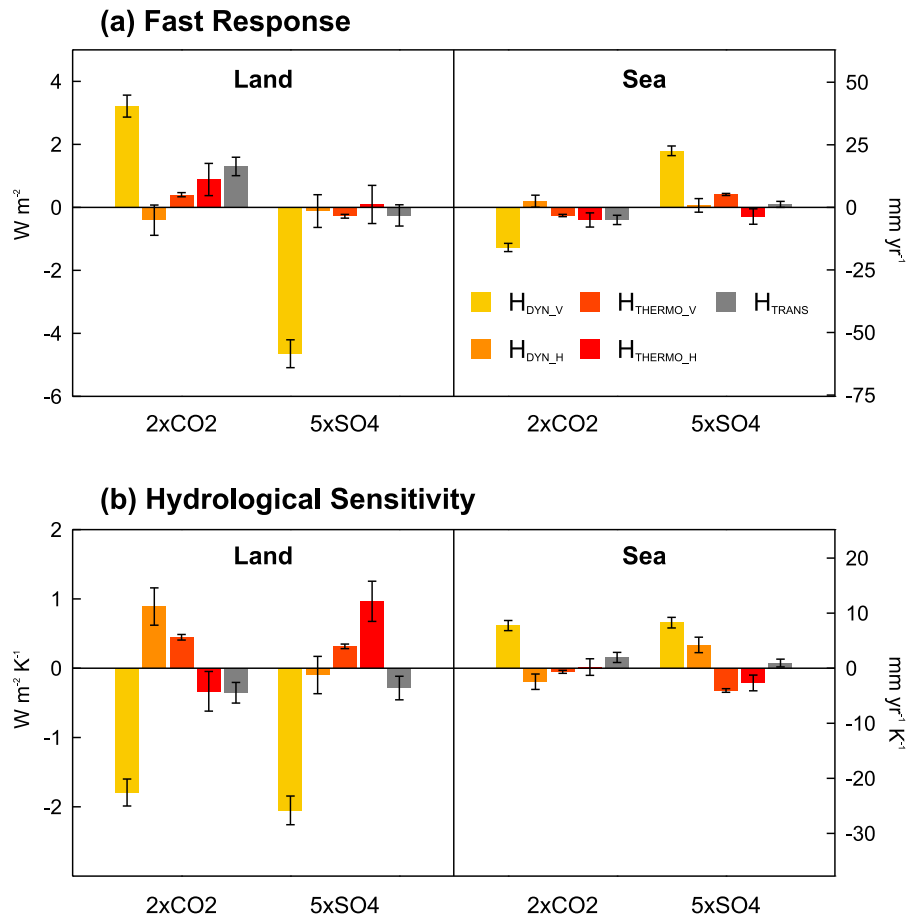


FIG. 4. Contributions to changes in land- and sea-mean DSE flux divergence due to changes in monthly mean vertical velocity (H_{DYN_v}), horizontal winds (H_{DYN_h}), vertical DSE gradients (H_{THERMO_v}), horizontal DSE gradients (H_{THERMO_h}), and transient eddy fluxes (H_{TRANS}) for HadGEM2. Results are shown for (a) the fast response and (b) the hydrological sensitivity for two forcing scenarios ($2\times CO_2$, $5\times SO_4$). Error bars denote the standard error due to interannual variability.

absorption combined with a shift of convection to over land. This is consistent with the findings from Chadwick et al. (2014) using a single model. A similar response is seen for $3\times CH_4$, but with a somewhat smaller magnitude.

The fast precipitation response over land in response to CO_2 exhibits the largest model spread of any forcing scenario (Fig. 2a). For all drivers, the intermodel spread in horizontal heat transport associated with circulation changes is strongly correlated with P_{fast} intermodel spread. For $2\times CO_2$, land SH flux intermodel spread is more strongly correlated with P_{fast} than for any other scenario ($r = -0.60$). This is likely due to the physiological effects of CO_2 , which affect stomatal closure leading to reduced evapotranspiration (Cao et al. 2010; Andrews et al. 2011; Pu and Dickinson 2014). This can be seen from the reduced latent heat (LH) flux from the surface over land (Fig. 5a), which also exhibits more

variability in response to CO_2 than any other driver. Given the dependency on physiological effects of the fast precipitation response to CO_2 over land, the importance of reducing uncertainty associated with vegetation schemes is evident. The global mean P_{fast} intermodel spread is even more dependent on land surface fluxes, with a cross-model correlation coefficient between land SH flux and global P_{fast} of -0.79 , as has also been seen in CMIP5 simulations (DeAngelis et al. 2016).

Changes in SO_4 and solar insolation drive the largest fast precipitation responses over land, despite having little effect on the global mean (Fig. 2a). When normalized by TOA forcing sulfate produces the largest fast response out of the five drivers (Fig. 3). The large response over land is associated with a large reduction in DSE flux divergence (Fig. 2a), indicating rapid changes in atmospheric circulation. The change in H for HadGEM2

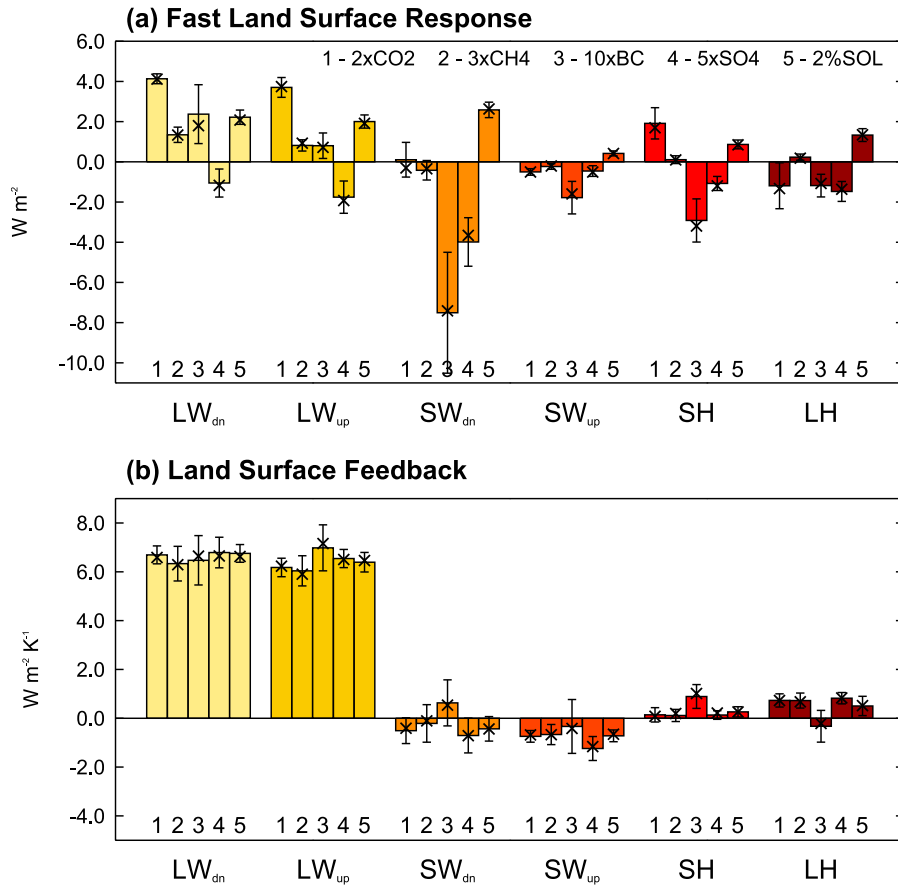


FIG. 5. Multimodel land-mean (a) fast response and (b) feedbacks for surface fluxes in response to the five PDRMIP forcing scenarios. Surface fluxes shown are downwelling longwave (LW_{dn}), upwelling longwave (LW_{up}), downwelling shortwave (SW_{dn}), upwelling shortwave (SW_{up}), sensible heat (SH), and latent heat (LH). Forcings are given in W m⁻², and feedbacks in W m⁻² K⁻¹. Error bars denote the standard deviation of model spread, and crisscrosses show the median value.

is predominantly due to a reduction in $H_{D_{yn,v}}$ (Fig. 4a), indicating a weakening of vertical motion over land. This is likely due to the strong reduction in downwelling SW radiation at the surface due to SO₄ (Fig. 5a). As a result, the land surface cools, resulting in a decrease in upwelling LW radiation and sensible and latent heat fluxes over land (Fig. 5a), therefore stabilizing the troposphere and inhibiting convection and precipitation over land. Unlike CO₂, there is very little effect on atmospheric radiative cooling and therefore the shift in precipitation from land to sea dominates. Increased insolation drives the opposite effect, with precipitation shifting from sea to land, consistent with the enhanced downwelling SW radiation at the surface. A small increase in atmospheric shortwave absorption results in a smaller magnitude fast precipitation response over land per unit TOA forcing than for sulfate.

Despite being shown to produce a large negative global mean fast precipitation response (Andrews et al.

2010; Samset et al. 2016), black carbon has very little effect on land mean precipitation (Fig. 2a). The reduction in precipitation is focused over the ocean. Atmospheric SW absorption increases significantly more over land than over sea (-9.5 and -4.4 W m⁻², respectively), presumably due to the higher concentrations of BC over land. However, the increase in SW absorption over land is largely offset by a decrease in SH flux, and an increase in LW cooling and DSE flux divergence. Increased LW cooling is expected in response to warming of the atmosphere. SW dimming at the surface combined with atmospheric warming will reduce surface SH flux. The increase in DSE flux divergence indicates that circulation adjustments occur that act to enhance precipitation over land. Black carbon is thought to affect large-scale monsoonal circulation patterns (Ramanathan and Carmichael 2008), particularly in India and South Asia (Ramanathan et al. 2005; Lau et al. 2006; Mehl et al. 2008; M.-K. Kim et al. 2016). Increased SW

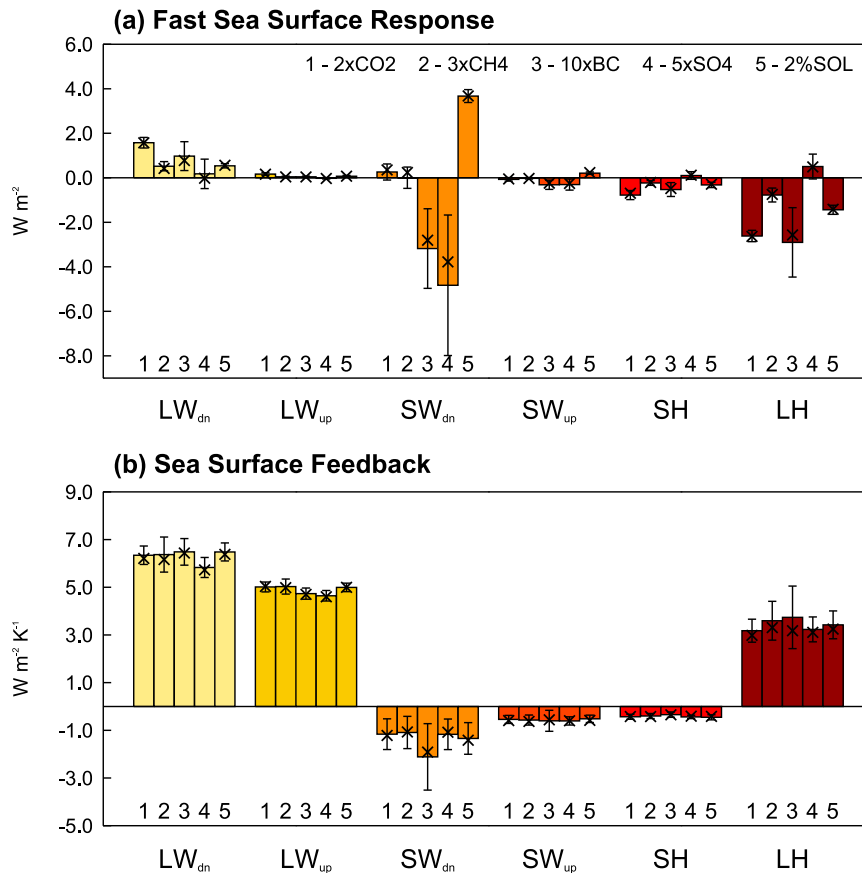


FIG. 6. As in Fig. 5, but for the sea-mean fast response and feedbacks.

absorption increases the atmospheric meridional heating gradient, thereby enhancing the South Asian monsoonal circulation (Lau et al. 2006; Meehl et al. 2008; M.-K. Kim et al. 2016), which is consistent with the increased DSE flux divergence over land. For the fast response there is no counteracting effect on circulation from changes in SST gradients. Over the oceans, the increased SW absorption dominates the fast response, resulting in a large decrease in precipitation.

As for the global $10\times\text{BC}$ response, the models with interactive chemistry introduce a large amount of model spread over both land and sea. In particular, there is a very large model spread in the SW absorption over land ranging from 5.0 to 15.0 W m^{-2} . Both the land and ocean fast responses per unit TOA forcing also exhibit larger uncertainties than for any other driver (Fig. 3). This demonstrates there is also considerable uncertainty in the response that is not due to different perturbations in concentration.

d. Hydrological sensitivity over land and sea

The hydrological sensitivity is considerably weaker over land than over sea for all scenarios (Fig. 2b). Excluding

$10\times\text{BC}$ (discussed below), the hydrological sensitivities over land and sea are fairly consistent between forcing scenarios, ranging from 8.0 to $15.1 \text{ mm yr}^{-1} \text{ K}^{-1}$ over land, and 38.1 to $43.1 \text{ mm yr}^{-1} \text{ K}^{-1}$ over sea (Fig. 2b). Despite the weaker land sensitivity, the radiative response is very similar, dominated by an increase in atmospheric LW cooling as temperature increases. There is also a small increase in SW absorption with warming. Temperature has little effect on sensible heat flux over land, whereas there is a small decrease in sensible heat flux with warming over the ocean.

The difference in hydrological sensitivity over land and sea is mainly associated with the horizontal energy transport (Fig. 2b). As global mean surface temperature increases, DSE flux divergence increases over the ocean and correspondingly decreases over land. In HadGEM2 the change in horizontal energy transport is mainly driven by a weakening of vertical motion over land and a strengthening over the ocean (Fig. 4b). This is consistent with limited moisture availability over land. Across models, the LH flux (evaporation) increases significantly with warming over the ocean (Fig. 6b), providing more moisture to fuel precipitation. However, over land LH

increases at a much slower rate, resulting in drying of the lower troposphere. Land-mean near-surface relative humidity decreases by -0.24 to $-0.72\% \text{ K}^{-1}$ across the forcing scenarios. The lack of moisture will likely inhibit moist convection, thus weakening vertical motion, and resulting in the lower land-mean hydrological sensitivity.

The hydrological sensitivity for $10\times\text{BC}$ is notably different from the other scenarios over both land and sea (Fig. 2b) and again exhibits the largest model spread. The surface temperature response to black carbon is small (Stjern et al. 2017), which will contribute to the high uncertainty. The multimodel mean surface temperature response to black carbon is 0.68 K , ranging from 0.16 to 1.66 K across models, with only two models producing a temperature change larger than 1 K . Therefore, as the responses are normalized by surface temperature change, in seven of the models the uncertainties are amplified. Over land there is an increase in SH flux and a much larger decrease in DSE flux divergence. Therefore the hydrological sensitivity is negative over land. Conversely, over the sea the hydrological sensitivity for $10\times\text{BC}$ is notably larger than for other drivers, associated with the larger DSE flux divergence.

e. Changes in global runoff

Changes in global runoff [precipitation minus evaporation ($P - E$) over land] are also an important aspect of the hydrological response to forcing. Previous studies suggest that global runoff increases with warming but at a smaller rate ($\sim 2.7\% \text{ K}^{-1}$) than expected from simple Clausius–Clapeyron scaling (Byrne and O’Gorman 2015). When the fast response is treated separately, as in the current study, the sensitivity of global runoff to temperature change is very small. The PDRMIP multimodel mean response ranges from -6.6 to $5.1 \text{ mm yr}^{-1} \text{ K}^{-1}$ (-2% to $2\% \text{ K}^{-1}$) across the forcing scenarios, lower than previous estimates. This is due to the weak land-mean precipitation sensitivity combined with increased land evaporation with warming (see the latent heat response in Fig. 5a). For all forcing scenarios except $3\times\text{CH}_4$, the fast response dominates long-term changes in global runoff. Doubling CO_2 drives a fast increase in global runoff of 16.0 mm yr^{-1} (6%). The large contribution of the fast response helps explain why changes in $P - E$ over land do not follow simple scalings with temperature change (Byrne and O’Gorman 2015). To fully understand changes in $P - E$ over land the short-time-scale nonlinear responses to climate forcings should be taken into account as well as temperature-driven effects.

f. Simple precipitation model

Based on the fast and slow components of precipitation change calculated from the PDRMIP simulations

we construct a simple model to estimate land-mean and sea-mean precipitation change (for model details, see section 2d). Precipitation change at any given time is estimated using a linear combination of forcing-dependent fast responses and a global-mean temperature-driven response (see Fig. 3 and Table S3). We use this simple model to emulate historical and future precipitation change over land and sea from 1850 to 2100 following RCP4.5 and RCP8.5 (Fig. 7).

The simple model matches well with the CMIP5 ensemble mean over both land and sea for the historical period and both future pathways. Lambert and Allen (2009) found that a simple regression-based energy budget model was unable to capture historical land precipitation changes for individual models. This may in part be due to inadequate information regarding the time series of black carbon (Pendergrass and Hartmann 2012). In addition, insufficiently representing land–sea energy transport through a single linear term may have contributed to discrepancies. In the current simple model land–sea energy transport is incorporated both in the fast components and the temperature-driven component. As shown in Fig. 2a, horizontal DSE flux divergence contributes strongly to the fast responses for all drivers. In addition, different R factors are used for each forcing agent included in the current model.

During the twentieth century there is very little long-term trend over the sea before a projected rise during the twenty-first century for both scenarios (Figs. 7b,d). The rate of increase is higher and more sustained for RCP8.5. Over land there is a small reduction in precipitation during the second half of the twentieth century before a projected increase during the twenty-first century for both scenarios (Figs. 7a,c). The predicted rate of increase is higher over the oceans than over the land. Good agreement between the simple model and the CMIP5 historical and future trends indicates that modeled precipitation change over land and sea can be well described using the fast and slow response framework. This enables us to isolate the contributions of each climate driver to precipitation change over land and sea as discussed below.

The simple model is also used to estimate observed land mean precipitation change from 1900 to 2015 using observed temperature records (Fig. 7e). This is compared with CRU TS and GPCC land mean precipitation records. Despite an observed global mean warming trend of $0.07 \text{ K decade}^{-1}$ from 1901 to 2010 (Morice et al. 2012), observations exhibit very little intensification of the hydrological cycle over land (Dai et al. 2009; Hartmann et al. 2013; Wu et al. 2013), as seen in Fig. 7e. The simple model also exhibits an insignificant land precipitation trend during the twentieth century when

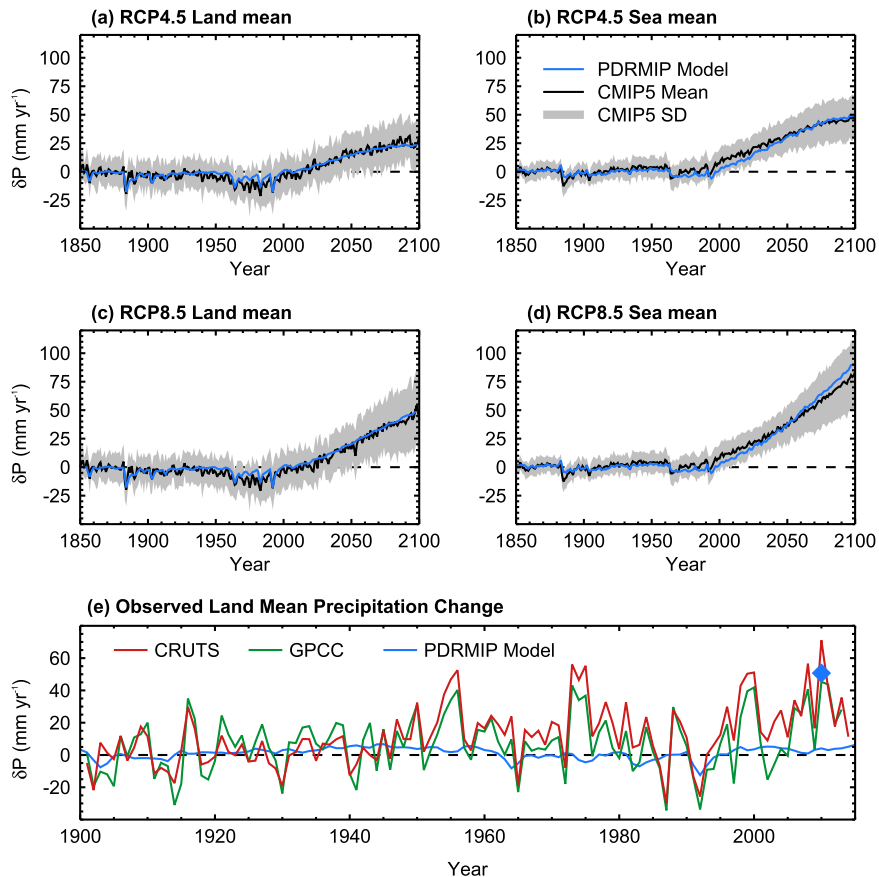


FIG. 7. Historical and future (a),(c) land-mean and (b),(d) sea-mean precipitation change relative to preindustrial for (top) RCP4.5 and (middle) RCP8.5, calculated using the CMIP5 multimodel mean (black), and simple PDRMIP model (blue). Light gray shading denotes the standard deviation of CMIP5 model spread. (e) The simple model (blue) is compared to observed land-mean precipitation change relative to the 1900–30 climatology, calculated using the CRU TS v.3.23 dataset (red) and the GPCC dataset (green). The blue diamond denotes the predicted precipitation change by the year 2100 using the simple model following RCP8.5. For details of the simple model formulation see section 2d. Uncertainties for the simple model estimates are shown in Table 1.

driven with observed temperatures. Anthropogenic aerosols are thought to have been important in reducing intensification of the global hydrological cycle over this period (Wu et al. 2013; Salzmann 2016). To understand why the modeled and observed trend is small, and to isolate which individual drivers are important over land and over sea, we can analyze the individual components of the simple model.

Despite the model and observations being consistent in exhibiting no significant trend in land precipitation during the twentieth century, it is clear from Fig. 7e that the simple model does not capture much of the observed interannual variability. This indicates that the processes controlling interannual variability may be different from the fast and slow processes driving the long-term trend represented in the simple model. Kramer and Soden

(2016) found that on global scales the sensitivity of the hydrological cycle to surface warming differs fundamentally between internal variability and anthropogenically forced changes. Clear-sky radiative processes were found to dominate the global hydrological response to anthropogenically driven warming, while cloud processes dominate internal variability.

Figure 8 shows the separate contributions to land-mean precipitation change in the simple model from fast responses to each forcing agent and the temperature-driven response between 1850 and 2100. The contributions of the different drivers at the end of the twentieth and twenty-first centuries relative to preindustrial are also given in Table 1. Over land during the twentieth century the positive influence of rising global mean temperature (red) is entirely cancelled out by the negative

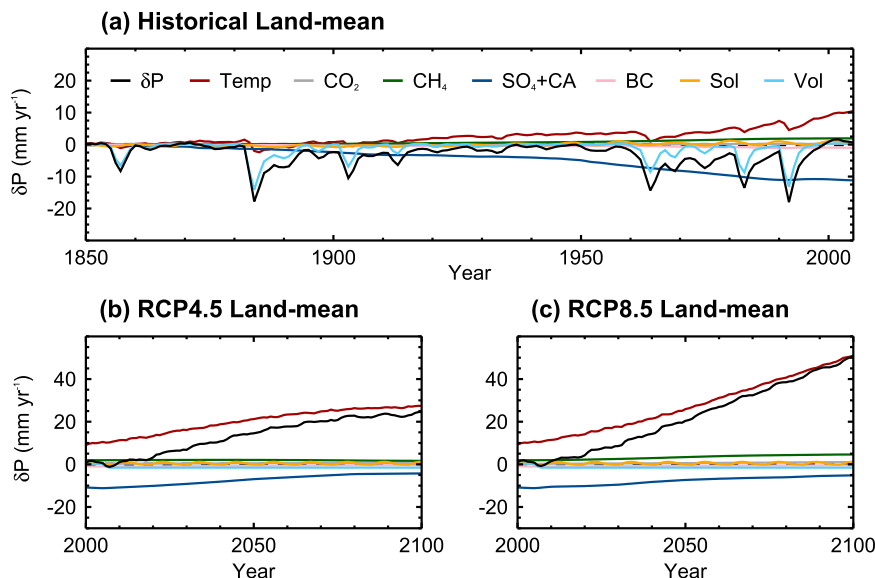


FIG. 8. Driver contributions to land-mean precipitation change relative to preindustrial during (a) the historical period and (b),(c) the future following RCP4.5 and RCP8.5, respectively, in the simple model. Colored lines indicate contributions from the fast response to carbon dioxide (CO_2 ; gray), methane (CH_4 ; green), sulfate and cloud albedo (SO_4+CA ; dark blue), black carbon (BC; pink), solar insolation (Sol; yellow), and volcanoes (Vol; light blue). Precipitation change driven by global mean surface temperature change is shown in red. Total precipitation change is shown in black. For details on methods see section 2d.

sulfate and cloud albedo fast responses (dark blue) (Fig. 8a). The combination of anthropogenic sulfate and volcanic forcing (light blue) drives a slight decrease in land mean precipitation between around 1950 and 1980. No other drivers strongly impact land mean precipitation through fast responses. Notably, CO_2 and black carbon have little direct impact on land mean precipitation, despite significantly weakening the increase in global mean precipitation (Thorpe and Andrews 2014; Frieler et al. 2011). The uncertainties associated with both the black carbon fast precipitation response and historical forcing are large (Bond et al. 2013). Therefore, black carbon could still play a significantly larger role than estimated here due to the associated uncertainties. However, the historical black carbon forcing would need to be a factor of 10 larger to drive the same magnitude changes in land-mean precipitation as sulfate forcing by the end of the twentieth century (see Table 1).

During the twenty-first century as sulfate concentrations decline, the rising global temperature increasingly dominates land mean precipitation change (Figs. 8b,c). As forcing-driven fast responses become less important during the twenty-first century, intensification of land precipitation should become more clearly observable. The interannual variability in the observations is large, with a detrended standard deviation of 16.6 and 17.3 mm for CRU TS and GPCC, respectively. However, the simple

model predicts that the increase in land mean precipitation from preindustrial levels will exceed the observational standard deviation by 2042 and 2055 for RCP8.5 and RCP4.5, respectively. Therefore, anthropogenically driven intensification of land precipitation may become more evident during the mid-twenty-first century.

The rate of increase in land precipitation is lower than over the sea, due to the weaker sensitivity of land precipitation to global temperature, consistent with limited moisture availability. Therefore, land-only based observations are not suited for inferring the global hydrological sensitivity to validate models.

Sea mean precipitation change also exhibits very little trend over the twentieth century (Fig. 9a), but there are different drivers counteracting the warming-driven intensification than seen for land. The influence of rising temperature is counteracted by the absorbing drivers, mainly CO_2 (gray) and black carbon (purple). During the twenty-first century, the rising global temperature increasingly dominates sea mean precipitation changes (Figs. 9b,c). However, the rate of increase in sea mean precipitation is limited by the negative CO_2 fast response, associated with reduced LW cooling.

4. Conclusions

We have presented the fast and slow responses of precipitation and the atmospheric energy budget to five

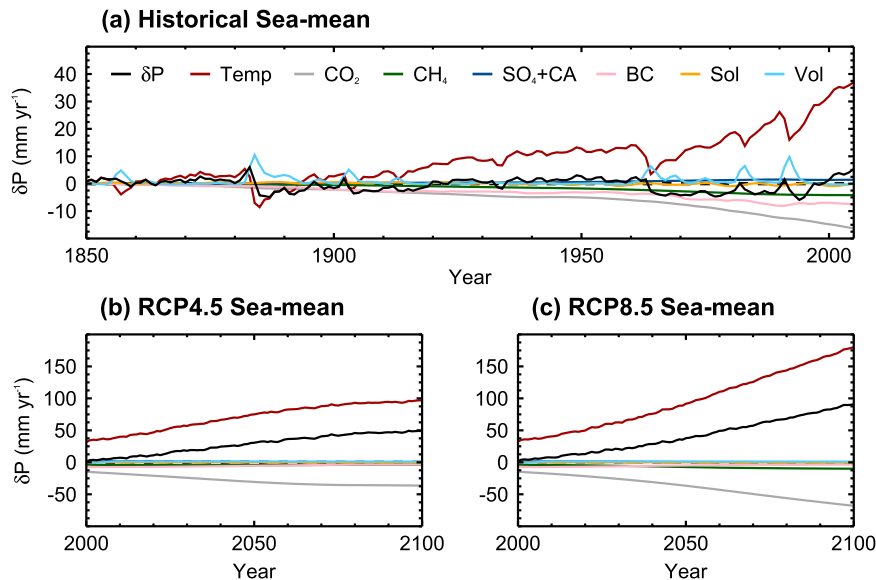


FIG. 9. As in Fig. 8, but for contributions to sea-mean precipitation change.

different forcings, across 10 global climate models. The response of global, land, and sea mean precipitation can be well understood through energetic arguments. When normalized by TOA forcing, CO_2 and black carbon produce the strongest global-mean fast responses due to enhanced atmospheric absorption reducing precipitation, but they also exhibit considerable model spread. For CO_2 , this can be traced to a variable land precipitation adjustment associated with uncertain changes in land-atmosphere heat fluxes, likely resulting from physiological effects. For black carbon, models with interactive chemistry introduce a large proportion of the spread, but there is also considerable uncertainty in the precipitation response to black carbon for a given TOA forcing. The global hydrological sensitivity is mainly associated with an increase in LW cooling, which is highly consistent across forcings, but contributes most strongly to the intermodel spread. There is a small increase in SW absorption with temperature, which exhibits very little spread across models.

Over land and sea, the fast and slow responses to forcing are very different. Over land, fast precipitation change is most sensitive to nonabsorbing or weakly absorbing drivers (e.g., SO_4 , solar). This is associated with the rapid land surface response affecting atmospheric stability and driving large circulation changes. For drivers that strongly affect atmospheric absorption (CH_4 , CO_2 , black carbon), the circulation changes are largely balanced by the changes in net atmospheric cooling. Over the sea, it is the absorbing drivers that produce the largest fast responses. The hydrological sensitivity is significantly smaller over land than over the

sea for all forcings, despite very similar changes in radiative cooling. The difference is associated with weakened vertical motion over land and enhanced vertical motion over the ocean, consistent with the limited moisture availability over land relative to the ocean.

Based on the fast and slow response framework, precipitation change over land and sea can be estimated using a linear combination of forcing-dependent fast responses and a temperature-driven response. This simple model can be used to disentangle the roles of the different forcing-driven fast responses and the temperature-driven response. The model, based on PDRMIP results, matches well with CMIP5 ensemble mean historical and future precipitation changes for RCP4.5 and RCP8.5. The simple model suggests that throughout the twentieth century the influence of rising global temperatures on land precipitation has been counteracted mainly by fast responses to anthropogenic sulfate and volcanic forcing. As a result, the estimated long-term trends are very small in comparison to the interannual variability seen in observations. Black carbon is estimated to have little effect on historical land-mean precipitation, but both the forcing and precipitation response are more uncertain than any other driver. During the twenty-first century, as sulfate forcing declines and global temperatures continue to rise, a sustained positive trend in land precipitation is expected. This suggests that anthropogenically driven intensification of land mean precipitation may become clearly evident by the mid-twenty-first century.

Over the ocean, the simple model suggests that fast responses to absorbing drivers (mainly CO_2 and black

carbon) have largely negated the influence on precipitation by rising temperatures during the twentieth century. During the twenty-first century the temperature-driven response increasingly dominates, leading to enhanced precipitation. Increasing CO₂ concentrations limit the rate at which precipitation increases due to the associated negative fast response. The projected rate of increase is higher over the sea than over land due to the considerably higher sensitivity to temperature change.

Acknowledgments. The PDRMIP model output is publicly available; for data access, visit <http://www.cicero.uio.no/en/PDRMIP/PDRMIP-data-access>. T.B.R. was supported by a NERC CASE award in collaboration with the Met Office NE/K007483/1. P.M.F. was supported by a Royal Society Wolfson Merit Award and NERC Grant NE/K006038/1. T.A. was supported by the Newton Fund through the Met Office Climate Science for Service Partnership Brazil (CSSP Brazil). B.H.S., G.M., and Ø.H. were funded by the Research Council of Norway, through the grant NApEX (229778). D.S. and G.F. thank NASA GISS for funding and acknowledge the NASA High-End Computing Program through the NASA Center for Climate Simulation at Goddard Space Flight Center for computational resources. O.B. acknowledges HPC resources from TGCC under the gencmip6 allocation provided by GENCI (Grand Equipement National de Calcul Intensif). T.T. is supported by the NEC SX-ACE supercomputer system of the National Institute for Environmental Studies, Japan, the Environmental Research and Technology Development Fund (S-12-3) of the Ministry of Environment, Japan, and JSPS KAKENHI Grants JP15H01728 and JP15K12190. M.K., D.S., and A.V. were supported by the Natural Environment Research Council under Grant NE/K500872/1, and by the Grantham Institute at Imperial College. Simulations with HadGEM2 and HadGEM3-GA4 were performed using the MONSooN system, a collaborative facility supplied under the Joint Weather and Climate Research Programme, which is a strategic partnership between the Met Office and the Natural Environment Research Council. D.O. and A.K. were supported by the Norwegian Research Council through the projects EVA (229771), EarthClim (207711/E10), NOTUR (nn2345k), and NorStore (ns2345k).

REFERENCES

- Alfieri, L., L. Feyen, F. Dottori, and A. Bianchi, 2015: Ensemble flood risk assessment in Europe under high end climate scenarios. *Global Environ. Change*, **35**, 199–212, <https://doi.org/10.1016/j.gloenvcha.2015.09.004>.
- Allen, M. R., and W. J. Ingram, 2002: Constraints on future changes in climate and the hydrologic cycle. *Nature*, **419**, 224–232, <https://doi.org/10.1038/nature01092>.
- Andrews, T., P. M. Forster, O. Boucher, N. Bellouin, and A. Jones, 2010: Precipitation, radiative forcing and global temperature change. *Geophys. Res. Lett.*, **37**, L14701, <https://doi.org/10.1029/2010GL043991>.
- , M. Doutriaux-Boucher, O. Boucher, and P. M. Forster, 2011: A regional and global analysis of carbon dioxide physiological forcing and its impact on climate. *Climate Dyn.*, **36**, 783–792, <https://doi.org/10.1007/s00382-010-0742-1>.
- Bala, G., K. Caldeira, and R. Nemani, 2010: Fast versus slow response in climate change: Implications for the global hydrological cycle. *Climate Dyn.*, **35**, 423–434, <https://doi.org/10.1007/s00382-009-0583-y>.
- Becker, A., P. Finger, A. Meyer-Christoffer, B. Rudolf, K. Schamm, U. Schneider, and M. Ziese, 2013: A description of the global land-surface precipitation data products of the Global Precipitation Climatology Centre with sample applications including centennial (trend) analysis from 1901–present. *Earth Syst. Sci. Data*, **5**, 71–99, <https://doi.org/10.5194/essd-5-71-2013>.
- Bond, T. C., and Coauthors, 2013: Bounding the role of black carbon in the climate system: A scientific assessment. *J. Geophys. Res.*, **118**, 5380–5552, <https://doi.org/10.1002/jgrd.50171>.
- Bony, S., G. Bellon, D. Klocke, S. Sherwood, S. Fermepin, and S. Denvil, 2013: Robust direct effect of carbon dioxide on tropical circulation and regional precipitation. *Nat. Geosci.*, **6**, 447–451, <https://doi.org/10.1038/ngeo1799>.
- Boucher, O., and Coauthors, 2016: Jury is still out on the radiative forcing by black carbon. *Proc. Natl. Acad. Sci. USA*, **113**, E5092–E5093, <https://doi.org/10.1073/pnas.1607005113>.
- Byrne, M. P., and P. A. O’Gorman, 2015: The response of precipitation minus evapotranspiration to climate warming: Why the “wet-get-wetter, dry-get-drier” scaling does not hold over land. *J. Climate*, **28**, 8078–8092, <https://doi.org/10.1175/JCLI-D-15-0369.1>.
- Cao, L., G. Bala, K. Caldeira, R. Nemani, and G. Ban-Weiss, 2010: Importance of carbon dioxide physiological forcing to future climate change. *Proc. Natl. Acad. Sci. USA*, **107**, 9513–9518, <https://doi.org/10.1073/pnas.0913000107>.
- Chadwick, R., I. Boutle, and G. Martin, 2013: Spatial patterns of precipitation change in CMIP5: Why the rich do not get richer in the tropics. *J. Climate*, **26**, 3803–3822, <https://doi.org/10.1175/JCLI-D-12-00543.1>.
- , P. Good, T. Andrews, and G. Martin, 2014: Surface warming patterns drive tropical rainfall pattern responses to CO₂ forcing on all timescales. *Geophys. Res. Lett.*, **41**, 610–615, <https://doi.org/10.1002/2013GL058504>.
- Chung, C. E., V. Ramanathan, and D. Decremer, 2012: Observationally constrained estimates of carbonaceous aerosol radiative forcing. *Proc. Natl. Acad. Sci. USA*, **109**, 11 624–11 629, <https://doi.org/10.1073/pnas.1203707109>.
- Dai, A., T. Qian, K. E. Trenberth, and J. D. Milliman, 2009: Changes in continental freshwater discharge from 1948 to 2004. *J. Climate*, **22**, 2773–2792, <https://doi.org/10.1175/2008JCLI2592.1>.
- DeAngelis, A. M., X. Qu, M. D. Zelinka, and A. Hall, 2015: An observational radiative constraint on hydrologic cycle intensification. *Nature*, **528**, 249–253, <https://doi.org/10.1038/nature15770>.
- , —, and A. Hall, 2016: Importance of vegetation processes for model spread in the fast precipitation response to CO₂

- forcing. *Geophys. Res. Lett.*, **43**, 12 550–12 559, <https://doi.org/10.1002/2016GL071392>.
- Dong, B., R. T. Sutton, E. Highwood, and L. Wilcox, 2014: The impacts of European and Asian anthropogenic sulfur dioxide emissions on Sahel rainfall. *J. Climate*, **27**, 7000–7017, <https://doi.org/10.1175/JCLI-D-13-00769.1>.
- Fläschner, D., T. Mauritsen, and B. Stevens, 2016: Understanding the intermodel spread in global-mean hydrological sensitivity. *J. Climate*, **29**, 801–817, <https://doi.org/10.1175/JCLI-D-15-0351.1>.
- Frieler, K., M. Meinshausen, T. Schneider von Deimling, T. Andrews, and P. Forster, 2011: Changes in global-mean precipitation in response to warming, greenhouse gas forcing and black carbon. *Geophys. Res. Lett.*, **38**, L04702, <https://doi.org/10.1029/2010GL045953>.
- Harris, I., P. D. Jones, T. J. Osborn, and D. H. Lister, 2014: Updated high-resolution grids of monthly climatic observations—The CRU TS3.10 dataset. *Int. J. Climatol.*, **34**, 623–642, <https://doi.org/10.1002/joc.3711>.
- Hartmann, D. J., and Coauthors, 2013: Observations: Atmosphere and surface. *Climate Change 2013: Physical Science Basis*, T. F. Stocker et al., Eds., Cambridge University Press, 159–254, <https://doi.org/10.1017/CBO9781107415324.008>.
- Held, I., and B. Soden, 2006: Robust responses of the hydrological cycle to global warming. *J. Climate*, **19**, 5686–5699, <https://doi.org/10.1175/JCLI3990.1>.
- Kim, M. J., S. W. Yeh, and R. J. Park, 2016: Effects of sulfate aerosol forcing on East Asian summer monsoon for 1985–2010. *Geophys. Res. Lett.*, **43**, 1364–1372, <https://doi.org/10.1002/2015GL067124>.
- Kim, M.-K., W. K. M. Lau, K. M. Kim, J. Sang, Y. H. Kim, and W. S. Lee, 2016: Amplification of ENSO effects on Indian summer monsoon by absorbing aerosols. *Climate Dyn.*, **46**, 2657–2671, <https://doi.org/10.1007/s00382-015-2722-y>.
- Kramer, R. J., and B. J. Soden, 2016: The sensitivity of the hydrological cycle to internal climate variability versus anthropogenic climate change. *J. Climate*, **29**, 3661–3673, <https://doi.org/10.1175/JCLI-D-15-0408.1>.
- Kvalevåg, M. M., B. H. Samset, and G. Myhre, 2013: Hydrological sensitivity to greenhouse gases and aerosols in a global climate model. *Geophys. Res. Lett.*, **40**, 1432–1438, <https://doi.org/10.1002/grl.50318>.
- Lambert, F. H., and N. E. Faull, 2007: Tropospheric adjustment: The response of two general circulation models to a change in insolation. *Geophys. Res. Lett.*, **34**, L03701, <https://doi.org/10.1029/2006GL028124>.
- , and M. R. Allen, 2009: Are changes in global precipitation constrained by the tropospheric energy budget? *J. Climate*, **22**, 499–517, <https://doi.org/10.1175/2008JCLI2135.1>.
- , M. J. Webb, M. Yoshimori, and T. Yokohata, 2014: The cloud radiative effect on the atmospheric energy budget and global mean precipitation. *Climate Dyn.*, **44**, 2301–2325, <https://doi.org/10.1007/s00382-014-2174-9>.
- Lau, K. M., M. K. Kim, and K. M. Kim, 2006: Asian summer monsoon anomalies induced by aerosol direct forcing: The role of the Tibetan Plateau. *Climate Dyn.*, **26**, 855–864, <https://doi.org/10.1007/s00382-006-0114-z>.
- Li, X., and M. Ting, 2017: Understanding the Asian summer monsoon response to greenhouse warming: The relative roles of direct radiative forcing and sea surface temperature change. *Climate Dyn.*, **49**, 2863–2880, <https://doi.org/10.1007/s00382-016-3470-3>.
- MacIntosh, C. R., R. P. Allan, L. H. Baker, N. Bellouin, W. Collins, Z. Mousavi, and K. P. Shine, 2016: Contrasting fast precipitation responses to tropospheric and stratospheric ozone forcing. *Geophys. Res. Lett.*, **43**, 1263–1271, <https://doi.org/10.1002/2015GL067231>.
- Meehl, G. A., J. M. Arblaster, and W. D. Collins, 2008: Effects of black carbon aerosols on the Indian monsoon. *J. Climate*, **21**, 2869–2882, <https://doi.org/10.1175/2007JCLI1777.1>.
- Meinshausen, M., and Coauthors, 2011: The RCP greenhouse gas concentrations and their extensions from 1765 to 2300. *Climatic Change*, **109**, 213–241, <https://doi.org/10.1007/s10584-011-0156-z>.
- Ming, Y., V. Ramaswamy, and G. Persad, 2010: Two opposing effects of absorbing aerosols on global-mean precipitation. *Geophys. Res. Lett.*, **37**, L13701, <https://doi.org/10.1029/2010GL042895>.
- Mitchell, J., C. Wilson, and W. Cunningham, 1987: On CO₂ climate sensitivity and model dependence of results. *Quart. J. Roy. Meteor. Soc.*, **113**, 293–322, <https://doi.org/10.1002/qj.49711347517>.
- Morice, C. P., J. J. Kennedy, N. A. Rayner, and P. D. Jones, 2012: Quantifying uncertainties in global and regional temperature change using an ensemble of observational estimates: The HadCRUT4 data set. *J. Geophys. Res.*, **117**, D08101, <https://doi.org/10.1029/2011JD017187>.
- Muller, C. J., and P. A. O’Gorman, 2011: An energetic perspective on the regional response of precipitation to climate change. *Nat. Climate Change*, **1**, 266–271, <https://doi.org/10.1038/nclimate1169>.
- Myhre, G., and B. H. Samset, 2015: Standard climate models’ radiation codes underestimate black carbon radiative forcing. *Atmos. Chem. Phys.*, **15**, 2883–2888, <https://doi.org/10.5194/acp-15-2883-2015>.
- , and Coauthors, 2013a: Radiative forcing of the direct aerosol effect from AeroCom Phase II simulations. *Atmos. Chem. Phys.*, **13**, 1853–1877, <https://doi.org/10.5194/acp-13-1853-2013>.
- , and Coauthors, 2013b: Anthropogenic and natural radiative forcing. *Climate Change 2013: The Physical Science Basis*, T. F. Stocker et al., Eds., Cambridge University Press, 659–740.
- , and Coauthors, 2017: PDRMIP: A Precipitation Driver and Response Model Intercomparison Project—Protocol and preliminary results. *Bull. Amer. Meteor. Soc.*, **98**, 1185–1198, <https://doi.org/10.1175/BAMS-D-16-0019.1>.
- O’Gorman, P. A., R. P. Allan, M. P. Byrne, and M. Previdi, 2012: Energetic constraints on precipitation under climate change. *Surv. Geophys.*, **33**, 585–608, <https://doi.org/10.1007/s10712-011-9159-6>.
- Pendergrass, A. G., and D. L. Hartmann, 2012: Global-mean precipitation and black carbon in AR4 simulations. *Geophys. Res. Lett.*, **39**, L01703, <https://doi.org/10.1029/2011GL050067>.
- , and —, 2014: The atmospheric energy constraint on global-mean precipitation change. *J. Climate*, **27**, 757–768, <https://doi.org/10.1175/JCLI-D-13-00163.1>.
- Previdi, M., 2010: Radiative feedbacks on global precipitation. *Environ. Res. Lett.*, **5**, 025211, <https://doi.org/10.1088/1748-9326/5/2/025211>.
- Pu, B., and R. E. Dickinson, 2014: Hydrological changes in the climate system from leaf responses to increasing CO₂. *Climate Dyn.*, **42**, 1905–1923, <https://doi.org/10.1007/s00382-013-1781-1>.
- Ramanathan, V., and G. Carmichael, 2008: Global and regional climate changes due to black carbon. *Nat. Geosci.*, **1**, 221–227, <https://doi.org/10.1038/ngeo156>.
- , and Coauthors, 2005: Atmospheric brown clouds: Impacts on South Asian climate and hydrological cycle. *Proc. Natl. Acad. Sci. USA*, **102**, 5326–5333, <https://doi.org/10.1073/pnas.0500656102>.

- Richardson, T. B., P. M. Forster, T. Andrews, and D. J. Parker, 2016a: Understanding the rapid precipitation response to CO₂ and aerosol forcing on a regional scale. *J. Climate*, **29**, 583–594, <https://doi.org/10.1175/JCLI-D-15-0174.1>.
- , B. H. Samsset, T. Andrews, G. Myhre, and P. M. Forster, 2016b: An assessment of precipitation adjustment and feedback computation methods. *J. Geophys. Res. Atmos.*, **121**, 11 608–11 619, <https://doi.org/10.1002/2016JD025625>.
- Salzmann, M., 2016: Global warming without global mean precipitation increase? *Sci. Adv.*, **2**, e1501572, <https://doi.org/10.1126/sciadv.1501572>.
- Samset, B. H., G. Myhre, and M. Schulz, 2014: Upward adjustment needed for aerosol radiative forcing uncertainty. *Nat. Climate Change*, **4**, 230–232, <https://doi.org/10.1038/nclimate2170>.
- , and Coauthors, 2016: Fast and slow precipitation responses to individual climate forcings: A PDRMIP multi-model study. *Geophys. Res. Lett.*, **43**, 2782–2791, <https://doi.org/10.1002/2016GL068064>.
- Seager, R., N. Naik, and G. A. Vecchi, 2010: Thermodynamic and dynamic mechanisms for large-scale changes in the hydrological cycle in response to global warming. *J. Climate*, **23**, 4651–4668, <https://doi.org/10.1175/2010JCLI3655.1>.
- Shaw, T. A., and A. Voigt, 2015: Tug of war on summertime circulation between radiative forcing and sea surface warming. *Nat. Geosci.*, **8**, 560–566, <https://doi.org/10.1038/ngeo2449>.
- Sherwood, S. C., S. Bony, O. Boucher, C. Bretherton, P. M. Forster, J. M. Gregory, and B. Stevens, 2015: Adjustments in the forcing-feedback framework for understanding climate change. *Bull. Amer. Meteor. Soc.*, **96**, 217–228, <https://doi.org/10.1175/BAMS-D-13-00167.1>.
- Shindell, D. T., and Coauthors, 2013: Radiative forcing in the ACCMIP historical and future climate simulations. *Atmos. Chem. Phys.*, **13**, 2939–2974, <https://doi.org/10.5194/acp-13-2939-2013>.
- Stjern, C. W., and Coauthors, 2017: Rapid adjustments cause weak surface temperature response to increased black carbon concentrations. *J. Geophys. Res. Atmos.*, **122**, 11 462–11 481, <https://doi.org/10.1002/2017JD027326>.
- Takahashi, K., 2009: The global hydrological cycle and atmospheric shortwave absorption in climate models under CO₂ forcing. *J. Climate*, **22**, 5667–5675, <https://doi.org/10.1175/2009JCLI2674.1>.
- Takemura, T., 2012: Distributions and climate effects of atmospheric aerosols from the preindustrial era to 2100 along representative concentration pathways (RCPs) simulated using the global aerosol model SPRINTARS. *Atmos. Chem. Phys.*, **12**, 11 555–11 572, <https://doi.org/10.5194/acp-12-11555-2012>.
- Thorpe, L., and T. Andrews, 2014: The physical drivers of historical and 21st century global precipitation changes. *Environ. Res. Lett.*, **9**, 064024, <https://doi.org/10.1088/1748-9326/9/6/064024>.
- Wu, P., N. Christidis, and P. Stott, 2013: Anthropogenic impact on Earth's hydrological cycle. *Nat. Climate Change*, **3**, 807–810, <https://doi.org/10.1038/nclimate1932>.